RESEARCH ARTICLE

"Three birds with one stone" nanoplatform: Efficient near-infrared-triggered type-I AIE photosensitizer for mitochondria-targeted photodynamic therapy against hypoxic tumors

Shengnan Liu[1] | **Yu Pei**[1] | **Yan Sun**[1] | **Ziwei Wang**[1] | **Haoran Chen**[2] |
Dongxia Zhu[1] | **Martin R. Bryce**[3] | **Ben Zhong Tang**[4,5] | **Yulei Chang**[2]

[1]Key Laboratory of Nanobiosensing and Nanobioanalysis at Universities of Jilin Province, Department of Chemistry, Northeast Normal University, Changchun, Jilin Province, People's Republic of China

[2]State Key Laboratory of Luminescence and Applications, Changchun Institute of Optics, Fine Mechanics and Physics, Chinese Academy of Sciences, Changchun, Jilin Province, People's Republic of China

[3]Department of Chemistry, Durham University, Durham, UK

[4]Department of Chemistry, Hong Kong Branch of Chinese National Engineering Research Center for Tissue Restoration and Reconstruction, State Key Laboratory of Molecular Neuroscience, Division of Life Science, Ming Wai Lau Centre for Reparative Medicine, Karolinska Institute, and Guangdong-Hong Kong-Macau Joint Laboratory of Optoelectronic and Magnetic Functional Materials, The Hong Kong University of Science and Technology, Kowloon, Hong Kong, People's Republic of China

[5]School of Science and Engineering, Shenzhen Institute of Aggregate Science and Technology, The Chinese University of Hong Kong, Shenzhen, Guangdong, People's Republic of China

Correspondence

Dongxia Zhu, Key Laboratory of Nanobiosensing and Nanobioanalysis at Universities of Jilin Province, Department of Chemistry, Northeast Normal University, 5268 Renmin Street, Changchun, Jilin Province 130024, People's Republic of China.
Email: zhudx047@nenu.edu.cn

Yulei Chang, State Key Laboratory of Luminescence and Applications, Changchun Institute of Optics, Fine Mechanics and Physics, Chinese Academy of Sciences, Changchun Jilin Province 130033, People's Republic of China.
Email: yuleichang@ciomp.ac.cn

Martin R. Bryce, Department of Chemistry, Durham University, Durham, DH1 3LE, UK.
Email: m.r.bryce@durham.ac.uk

Ben Zhong Tang, Department of Chemistry, Hong Kong Branch of Chinese National Engineering Research Center for Tissue Restoration and Reconstruction, State Key Laboratory of Molecular Neuroscience, Division of Life Science, Ming Wai Lau Centre for Reparative Medicine, Karolinska Institute, and Guangdong-Hong Kong-Macau Joint Laboratory of Optoelectronic and Magnetic Functional Materials, The Hong Kong University of Science and Technology, Kowloon, Hong Kong 999077, People's Republic of China.
Email: tangbenz@cuhk.edu.cn

Abstract

Currently three major problems seriously limit the practical application of cancer photodynamic therapy (PDT): (i) the hypoxic tumor microenvironment (TME); (ii) low generation efficiency of toxic reactive oxygen species (ROS) in aggregates and (iii) shallow tissue penetration depth of excitation light. Very limited approaches are available for addressing all the above three problems with a single design. Herein, a rational "three birds with one stone" molecular and nanoengineering strategy is demonstrated: a photodynamic nanoplatform **U-Ir@PAA-ABS** based on the covalent combination of lanthanide-doped upconversion nanoparticles (UCNPs) and an AIE-active dinuclear Ir(III) complex provides a low oxygen concentration-dependent type-I photochemical process upon 980 nm irradiation by Föster resonance energy transfer (FRET). **U-Ir@PAA-ABS** targets mitochondria and has excellent phototoxicity even in severe hypoxia environments upon 980 nm irradiation, inducing a dual-mode cell death mechanism by apoptosis and ferroptosis. Taken together, the in vitro and in vivo results demonstrate a successful strategy for improving the efficacy of PDT against hypoxic tumors.

KEYWORDS

hypoxia tumor, iridium complex, nanoplatform, near-infrared photosensitizer, photodynamic therapy, type-I photosensitizer

1 | INTRODUCTION

Photodynamic therapy (PDT) capitalizes on a combination of localized external light, photosensitizers (PSs) and oxygen (O_2) to produce highly toxic reactive oxygen species (ROS) to fulfill the desired therapeutic effects. PDT is a clinically approved treatment for malignant tumors due to its time-space specificity, noninvasive nature and high biocompatibility.[1–4] Additionally, recent research has demonstrated that PDT can also reduce glutathione (GSH) antioxidant levels and induce ferroptosis (an intracellular iron-dependent form of cell death), which further broadens the application scope of PDT.[5,6] Although PDT has witnessed rapid development, the scarcity of an optimal PS to meet the multiple criteria of cancer treatment still restricts clinical applications.[7] Currently, conventional PSs act mainly through high-O_2-dependence type-II energy transfer processes.[8,9] Hypoxia (i.e., oxygen deprivation) is an intrinsic characteristic of malignant solid tumors, and is an urgent problem to be solved for clinical PDT efficacy.[10–12] Many strategies have targeted this problem, but they are still in their infancy.[13–15] One strategy is delivering O_2 or generating O_2 in situ, which has benefits, but with unsatisfactory stability and safety.[14] Alternatively, recent studies disrupt the hypoxia-inducible factors-1α (HIF-1α, a decisive mediator of the hypoxic response mechanism) to improve tumor oxygenation and ameliorate the hypoxia tumor microenvironment (TME).[16–18] However, the major strategy is to exploit a type-I PDT process,[11,19] to transmit electrons to various tissue substrates to generate cytotoxic ROS species such as superoxide anion radical ($O_2^{-\bullet}$), hydrogen peroxide (H_2O_2) and hydroxyl radical ($\bullet OH$).[20,21] Specifically, $O_2^{-\bullet}$ can further regenerate oxygen through dismutation under superoxide dismutase, eventually arriving at diminished O_2 dependence, thereby displaying huge potential in overcoming tumor hypoxia.[21,22] However, the antitumor performance of most reported type-I PSs, like bacteriochlorins[23] and benzophenothiazine,[22] is greatly compromised owing to their reduced ROS generation in aggregates.[24] Thus, alleviating the impact of hypoxic TME for PDT is still a formidable challenge.

A key factor for efficient PDT is a long-lived excited triplet state (T_1) of the PS for enhancing the ROS generation.[7] PSs with aggregation-induced emission (AIE) are beneficial for promoting a high intersystem crossing (ISC) rate and thereby increasing their ROS-generating efficiency in aggregated states.[20,25,26] The enhanced spin-orbit coupling favored by the heavy atom effect in transition metal complexes (such as Ir(III) complexes) could also increase the ISC rate, which is not easily achieved by organic PSs.[27–29] Moreover, the electronic excited states of some transition metal complexes upon light irradiation promote the electron transfer pathway and facilitate the type-I photodynamic activity.[13] Unfortunately, most Ir complexes are excited only by blue or visible light[30] in the blue-green window with shallow tissue penetration (<4 mm)[31] which limits PDT treatment to surface tumors.[32] To circumvent this drawback, great efforts have been devoted to constructing PSs to treat deep-seated tumors by excitation with near-infrared (NIR) light.[33] However, Ir complex PSs with NIR-excitation are still rare, especially AIE-Ir complexes, which need a rigid structure to reduce the vibrational relaxation rate, requiring an intricate molecular design strategy.[34]

PSs with long-wavelength optical excitation windows (e.g., >850 nm) are scarce, primarily because fast non-radiative deactivation pathways caused by intramolecular vibrational relaxation shorten the T_1 lifetime, thereby reducing ROS generation.[34–36] Given these circumstances, photon upconversion nanoparticles (UCNPs) are used to overcome the penetration depth limit caused by visible light that is needed for traditional PDT to activate PSs. Thulium-activated UCNPs can convert the NIR photons to UV–vis photons and thereby in situ excite the surface-anchored PSs through Föster resonance energy transfer (FRET), which surmounts the impediment of light penetration depth in PDT procedures.[37–40] Based on the above discussion, a "three birds with one stone" strategy, namely (i) NIR light irradiation, (ii) relieved hypoxia and (iii) excellent ROS generation ability of PSs, will be a breakthrough for effective PDT development.

Herein, we use molecular and nanoengineering to address the above issues. UCNPs are covalently bonded with a tailor-made AIE-active dinuclear Ir(III) complex (named **Ir complex**) and carbonic anhydrase IX (CA IX) inhibitor 4-(2-aminoethyl) benzenesulfonamide (**ABS**)[41] to form **U-Ir@PAA-ABS** nanophotosensitizer (Scheme 1). Covalent coupling of the PSs onto the UCNPs' surface should shorten the distance between the UCNPs and the PSs, thereby boosting the energy transfer efficiency and enhancing the ROS generation.[42–44] The inhibitory effect of CA IX effectively relieves tumor hypoxia because of the inhibition of HIF-1α expression.[15,45,46] **U-Ir@PAA-ABS** shows potential for synergistic dual-mode PDT of type-I ($O_2^{-\bullet}$) and type-II (singlet oxygen, $^1O_2$) under 980 nm irradiation. In vitro experiments indicate that **U-Ir@PAA-ABS** targets mitochondria and possesses high intracellular phototoxicity, whether in normoxia or hypoxia conditions. **U-Ir@PAA-ABS** inhibits the expression of CA IX and HIF-1α, contributing to the generation of type-I ROS in hypoxic cells, further promoting photo-cytotoxicity, and suppressing ferroptosis resistance. Furthermore, photoirradiation on the nanoplatform causes multi-mode cell death mechanisms of apoptosis and ferroptosis in MDA-MB-231 cells. In vivo experiments have shown that **U-Ir@PAA-ABS** significantly inhibits tumor growth after intravenous injection in 4T1-bearing mice models upon 980 nm irradiation. This work provides a benchmark for designing NIR light-triggered PSs to deal with hypoxic TME and to achieve efficient applications in deep-seated tumor phototherapy.

2 | RESULTS AND DISCUSSION

2.1 | Design, synthesis, and characterization of Ir complex and UCNPs

Ir complex was synthesized through conventional methods (Schemes S1 and S2 in Supporting Information). The bimetallic complex with a Schiff base bridging ligand was chosen because of the known ease of synthesis of this framework and its bright red-shifted emission induced by aggregation.[47] The carboxylic acid
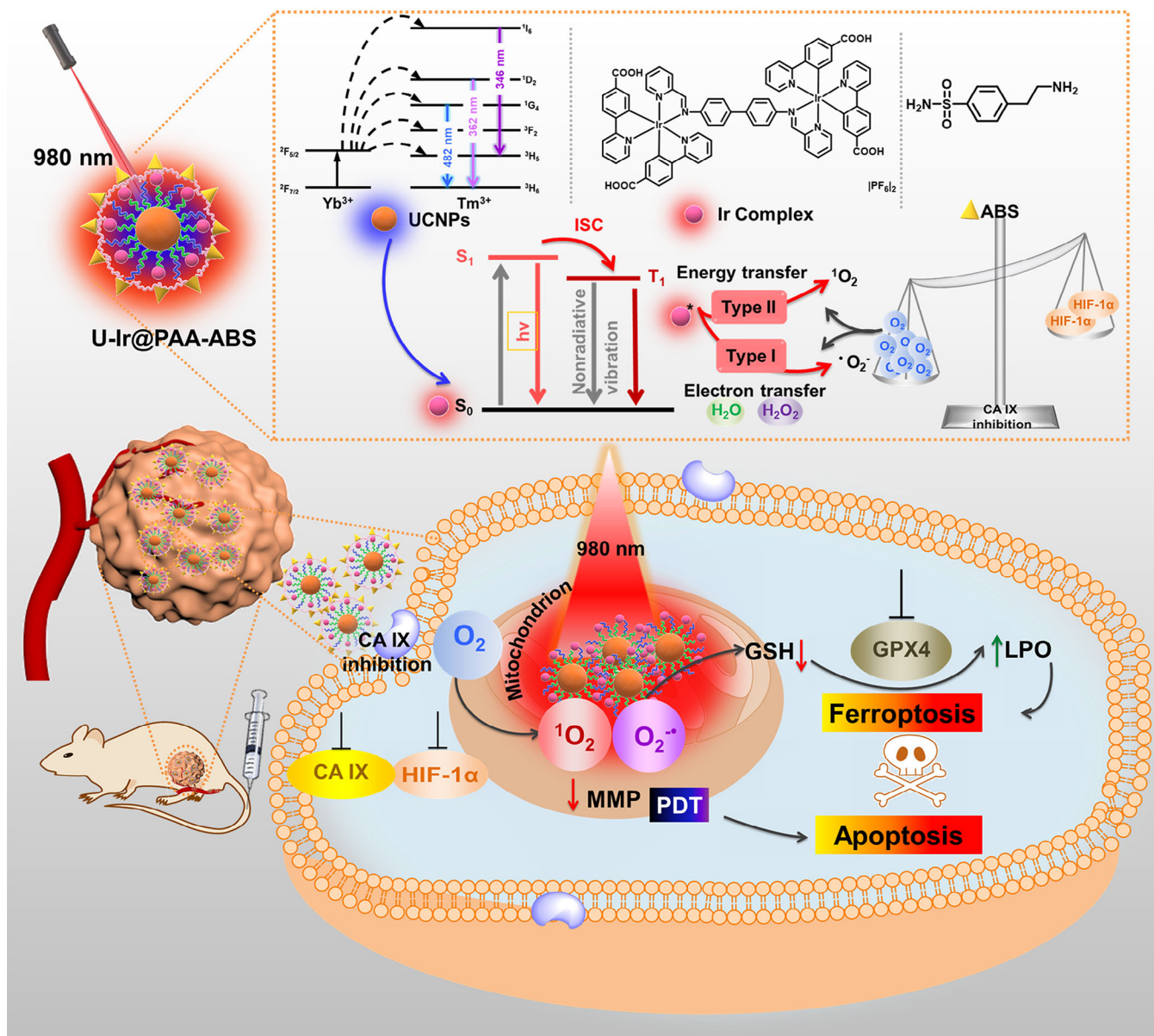
SCHEME 1 Schematic illustration of **U-Ir@PAA-ABS** for mitochondria-targeted PDT against hypoxic tumors.

groups on the ligands enable covalent bonding to the UCNPs.[43] The molecular structure was validated by proton nuclear magnetic resonance (^{1}H NMR) spectroscopy, mass spectrometry (Figures S1–S5) and elemental analysis. The efficient host-sensitized multiphoton UCNPs (LiYbF$_4$@LiYb/Tm(99.5%/0.5%)F$_4$@LiYF$_4$) were prepared as in our previous report (Supporting Information)[39] and their energy-dispersive X-ray (EDX) spectra are shown in Figure S6.
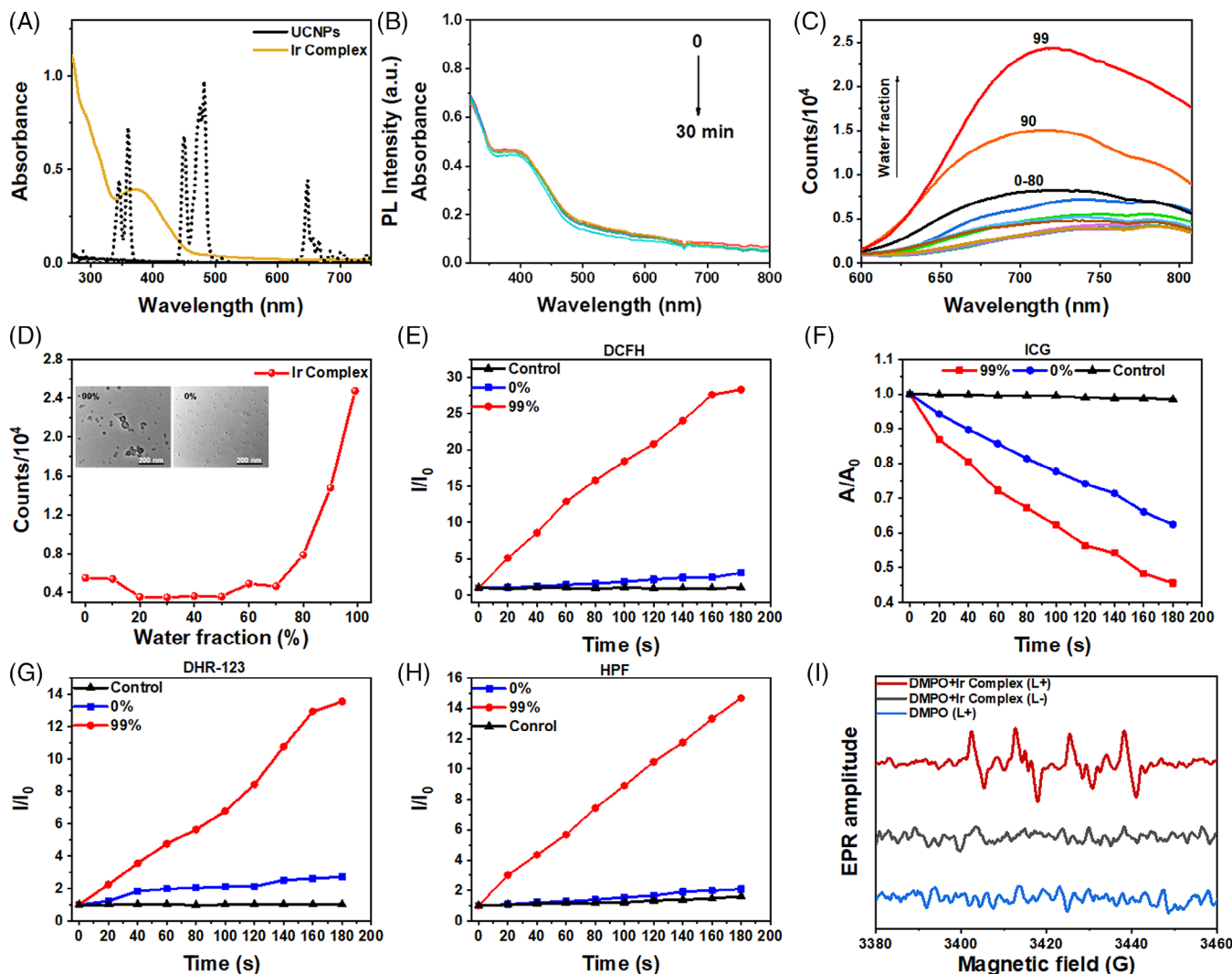
The photophysical properties of the **Ir complex** and the UCNPs are shown in Figure 1A, and the corresponding photophysical data of the **Ir complex** are summarized in Table S1. The **Ir complex** has absorption bands in the UV (250–350 nm) and blue light regions (weak band, 350–500 nm), assigned to the mixed singlet and triplet metal-to-ligand charge-transfers (^{1}MLCT and ^{3}MLCT) and intraligand (π–π*) transitions (C^N ligands). There is bright deep-red emission at 720 nm (high quantum yield of fluorescence, PLQY = 24.70%). Meanwhile, upon 405 nm irradiation, **Ir complex** exhibits good photostability, which is one of

the most important criteria for PSs (Figure 1B).[48,49] In the photoluminescence (PL) spectra, no obvious emission of **Ir complex** was observed in MeOH solution, while the emission intensity was greatly enhanced when water fractions (f_w) reached 99% (Figure 1C,D) owing to restriction of intramolecular motion (RIM), indicating an excellent AIE feature. According to a previous report, PSs with AIE enhance ROS generation in the aggregated state,[26] allowing **Ir complex** to be an excellent PS.

2.2 | ROS generation ability of Ir complex

To verify the potential for PDT applications, 2′,7′-dichlorodihydrofluorescein (DCFH) was used as a probe for ROS generation. As shown in Figure 1E and Figure S8, the emission peak of DCFH at 525 nm increases in the presence of **Ir complex** upon exposure to blue light compared with the control group. Moreover, the aggregated-form **Ir complex** (f_w: 99%) represents better ROS generation
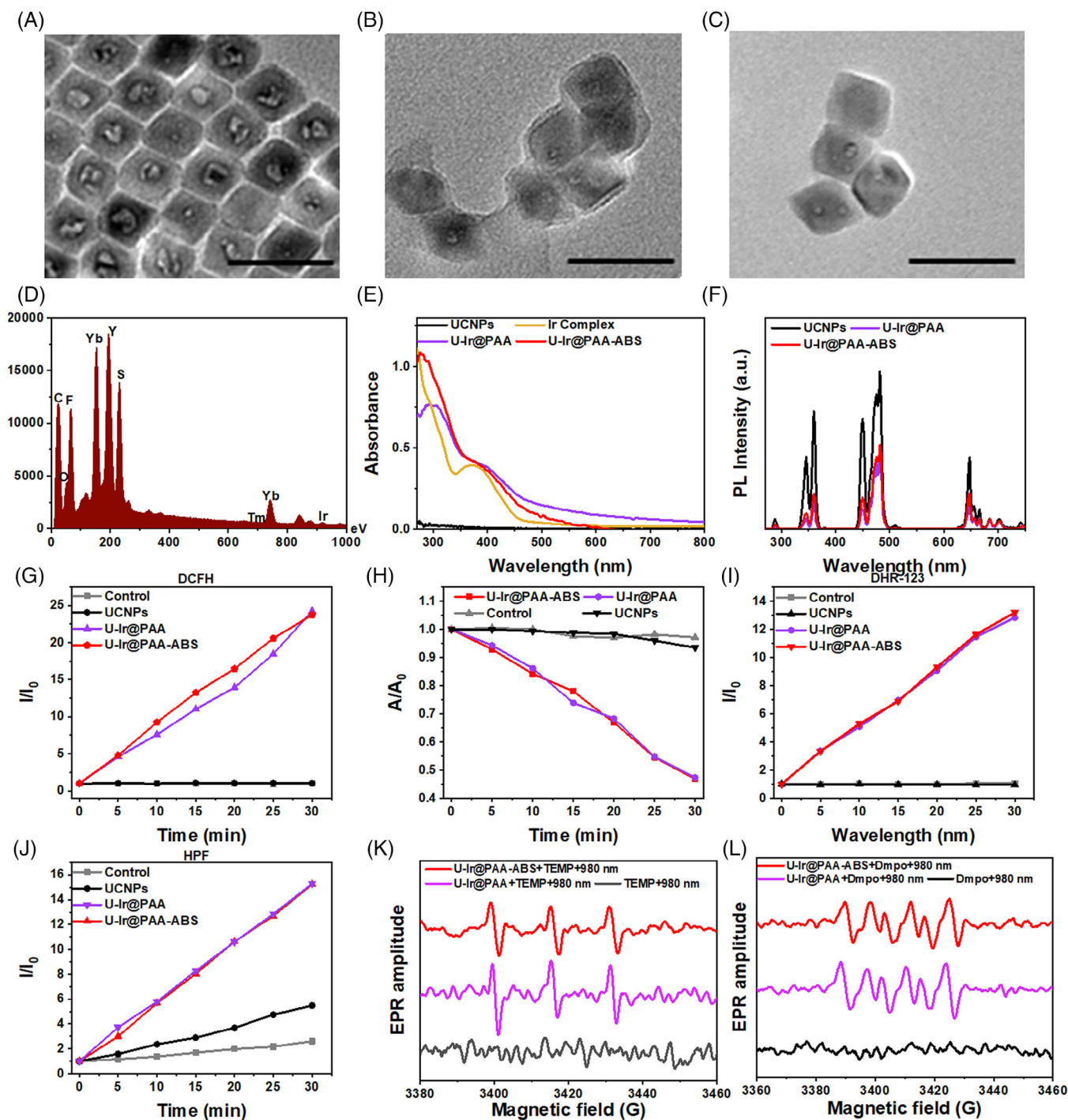
FIGURE 1 The photophysical properties and ROS production ability of Ir complex. (A) The absorption and emission spectra of **Ir complex** and **UCNPs**, and the emission spectra of **UCNPs**. (B) UV–vis absorption spectral changes of **Ir complex** upon exposure to LED light (405 nm, 20 mW cm^{-2}) for 30 min. (C) Emission spectra of **Ir complex** in MeOH-H$_2$O mixtures (complex concentration = 1.0×10^{-5} M) with different water fractions (0%–99% v/v) at room temperature. (D) The change of the emission intensity of **Ir complex** in MeOH-H$_2$O with the change of the water concentration. Inset: TEM image of **Ir complex** when the water fraction is 0% and 99%. The change of PL intensity of DCFH (E) and DHR 123 (G) with the change of time under different conditions. I_0 = initial intensity of 525 nm. I = real-time intensity of 525 nm with various times of light exposure. (F) The decay rates of ICG under different conditions. A_0 = initial absorbance of 790 nm. A = real-time absorbance of 790 nm with various times of light exposure. (H) The change of PL intensity of HPF with the change of time under different connditions. I_0= initial intensity of 515 nm. I= real-time intensity of 515 nm with various times of light exposure. (I) EPR signals of DMPO (for type-I ROS detection) in the presence of **Ir complex** in the absence (L-) and presence (L+) of LED light (405 nm, 20 mW cm^{-2}).

ability ($I/I_0 \approx 28$) than free **Ir complex** (fw: 0%) ($I/I_0 \approx 3$), which should be attributed to the beneficial reduction in nonradiative transitions caused by the aggregation-induced RIM effect, resulting in an increase in the T$_1$ of **Ir complex** and hence increased ROS generation. Furthermore, indocyanine green (ICG), dihydrorhodamine 123 (DHR 123) and hydroxyphenyl fluorescein (HPF) were used to detect ROS types. In Figure 1F and Figure S9, the degradation of ICG at 790 nm is nearly 60% in the presence of **Ir complex** upon exposure to blue light indicating its excellent $^1O_2$ generation ability. According to Figure 1G and Figure S10, the emission of DHR 123 rapidly increases to ≈15 times of the original value in the presence of **Ir complex** under blue LED, which reveals the outstanding O$_2^{-\bullet}$ generation capacity of **Ir complex**. Meanwhile, **Ir complex** also shows •OH generation ability under blue light irradiation compared with the control group (Figure 1H and Figure S11). Moreover, 5,5-dimethyl-1-pyrroline-N-oxide (DMPO) was used

as a probe for type-I ROS generation. Electron paramagnetic resonance (EPR) signals were observed after irradiation of DMPO + **Ir complex**, indicating free radical formation. In contrast, there were no clear signals from DMPO under light or from DMPO + **Ir complex** in darkness, establishing that **Ir complex** also exhibits type-I ROS generation (Figure 1I). These results confirm that **Ir complex** underwent both types-I and II-based ROS processes under irradiation, especially with less oxygen dependence in the type-I process, which favors inhibiting hypoxic tumor cells.

2.3 | Design, preparation, and characterization of the nanoplatforms

To obtain efficient NIR-activated PSs, **Ir complex** was covalently bonded to the UCNPs to construct **U-Ir** NPs (SI). The FT-IR spectra show the peak changes at 3420 cm^{-1} and

FIGURE 2 The photophysical properties and ROS production ability of **U-Ir@PAA** and **U-Ir@PAA-ABS**. TEM images of (A) **UCNPs**, (B) **U-Ir@PAA** and (C) **U-Ir@PAA-ABS**; Scale bars = 50 nm. (D) EDX spectrum of **U-Ir@PAA-ABS**. (E) The absorption spectra of **Ir complex**, **UCNPs**, **U-Ir@PAA** and **U-Ir@PAA-ABS**. (F) The emission spectra of **UCNPs**, **U-Ir@PAA** and **U-Ir@PAA-ABS**. The change of PL intensity of DCFH (G) and DHR 123 (I) with the change of time under different conditions. I_0 = initial intensity of 525 nm. I = real-time intensity of 525 nm with various times of light exposure. (H) The decay rates of ABDA under different conditions. A_0 = initial absorbance of 378 nm. A = real-time absorbance of 378 nm with various times of light exposure. (J) The change of PL intensity of HPF with the change of time under different conditions. I_0 = initial intensity of 515 nm. I = real-time intensity of 515 nm with various times of light exposure. EPR signals of TEMP (for type-II ROS detection) (K) and DMPO (for type-I ROS detection) (L) in the presence of **U-Ir@PAA** and **U-Ir@PAA-ABS** in DMSO (980 nm, 0.7 W cm^{-2}).

the C=O peak in the amide region appears at 1716 cm^{-1}, demonstrating that **Ir complex** is successfully attached to the surface of the UCNPs (Figure S13). The transmission electron microscopy (TEM) image confirms the average size of the oleic acid-capped UCNPs to be ≈22 nm (Figure 2A). The **U-Ir** was encapsulated by polyacrylic acid (**PAA**) through electrostatic incorporation to form **U-Ir@PAA** (Figure 2B). EDX spectroscopy revealed the elements in **U-Ir@PAA** as C,

O, F, Yb, Y, Tm, Ir (Figure S6). Furthermore, **ABS** was introduced into the nanoplatform to inhibit CA IX (Supporting Information). **ABS** is amide-bonded to **PAA**, and the peaks in the FT-IR spectra located at 1550 cm^{-1} and 1156 cm^{-1} in **U-Ir@PAA-ABS** compared with **U-Ir** indicate the successful incorporation of **ABS-PAA** (Figure S13). The loading content of **Ir complex** was determined to be 12.8 wt% by UV–vis analysis (Figure S7). The organic polymer shell of

U-Ir@PAA-ABS was directly observed in the TEM image (Figure 2C), and the elements in **U-Ir@PAA-ABS** are C, O, F, S, Yb, Y, Tm and Ir, as shown by EDX spectroscopy (Figure 2D). The hydrodynamic size and polydispersity index (PDI) of **U-Ir@PAA** and **U-Ir@PAA-ABS** measured by dynamic light scattering (DLS) are shown in Figure S14. Sizes were 177.3 nm and 153.2 nm, respectively. The zeta potentials of **U-Ir@PAA** and **U-Ir@PAA-ABS** are −20.0 and −29.0, respectively (Figure S15). Besides, the PL intensity of **U-Ir@PAA-ABS** and **U-Ir@PAA** were similar to the aggregated (fw: 95%) **Ir complex**, which emits brighter than the free (fw: 0%) Ir complex ($I/I_0 > 2$) indicating that Ir complexes are still aggregated after the covalent attachment to UCNPs to show AIE characteristics (Figure S16). There was no significant change in the size of the nanoparticles within 6 days, indicating their excellent stability (Figure S14c).

LiYbF$_4$@LiYbF$_4$:Tm(0.5%)@LiYF$_4$ were selected as fluorescence donors due to the large spectral overlap between their emission and the high energy absorption bands of **Ir complex** which will ensure efficient energy transfer (Figures 1A and 2E). Compared with the **UCNPs**, the peak in the UV and the blue band are reduced in the PL spectra of **U-Ir@PAA** and **U-Ir@PAA-ABS** owing to the strong absorption by **Ir complex** via energy transfer (Figure 2F). The energy lifetimes of **UCNPs** and **U-Ir@PAA-ABS** excited states measured at 362 and 482 nm were shortened, implying FRET between the **UCNPs** and **Ir complex** (Figure S17). Both **U-Ir@PAA** and **U-Ir@PAA-ABS** exhibit excellent photostability under 980 nm irradiation (Figure S18).

2.4 | ROS generation ability of nanoplatforms

To verify the PDT potential of the nanoplatform, DCFH was used to probe the ROS generation ability of the nanoplatforms, and the indicator with 980 nm irradiation and ROS generation capacity of UCNPs were investigated as control groups. The emission peak of DCFH at 525 nm in the presence of **U-Ir@PAA** and **U-Ir@PAA-ABS** upon 980 nm irradiation, shown in Figure S21 and Figure 2G, increased to more than 20 times compared to control groups, indicating excellent photoirradiated ROS generation ability of the nanoplatforms. To further verify the tissue penetration ability of the NIR excited nanoplatform, the ROS generation ability of **Ir complex** (light source: 405 nm) and **U-Ir@PAA-ABS** (light source: 980 nm) was detected by DCFH with the coverage of different depths of intralipid. As shown in Figure S22, the ROS generation of 405 nm irradiated **Ir complex** rapidly decreased with 1 mm penetration depth, while 980 nm irradiated **U-Ir@PAA-ABS** still produced ROS with an acceptable yield. When the penetration depth increased to 2.5 mm, 405 nm irradiated **Ir complex** generated almost no ROS, yet 980 nm irradiated **U-Ir@PAA-ABS** possesses ROS generation ability. These results indicate that the NIR excitation nanoplatform has stronger tissue penetration ability to generate ROS, making it a promising PS for antitumor applications.

In addition, 9,10-anthracenediyl-bis(methylene)dimalonic acid (ABDA), DHR 123 and HPF were used to distinguish the ROS types. In Figure S23, the absorption band of ABDA at 378 nm decreased by >50% in the presence of **U-Ir@PAA** and **U-Ir@PAA-ABS** under 980 nm irradiation within 30 min, implying the excellent $^1O_2$ generation ability of the nanoplatforms. Under 980 nm irradiation the emission of DHR 123 in the presence of **U-Ir@PAA** and **U-Ir@PAA-ABS** rapidly increased to ≈15 times the original value suggesting their $O_2^{-\bullet}$ generation capacity (Figure S24 and Figure 1G). According to Figure S25 and Figure 1J, using HPF as a probe, **U-Ir@PAA** and **U-Ir@PAA-ABS** produce •OH under photoirradiation compared with the control groups. Furthermore, EPR spectroscopy was conducted to probe ROS generation of the nanoplatforms. DMPO and 2,2,6,6-tetramethylpiperidine (TEMP) were used as spin-traps to quantify the type-I and type-II ROS, respectively. The data confirm that upon NIR irradiation **U-Ir@PAA** and **U-Ir@PAA-ABS** are excellent producers of type-I and type-II ROS compared with the control group (Figure 2K,L). Under 980 nm irradiation, the UV and blue light emitted by the **UCNPs** is absorbed by **Ir complex** via FRET, and the **Ir complex** T$_1$ state generates type-I and type-II ROS through electron transfer and energy transfer, respectively. The above mechanism promotes the application of **U-Ir@PAA-ABS** in vitro and in vivo.

## 2.5 | Cellular uptake and subcellular accumulation

The in vitro performance of **U-Ir@PAA-ABS** was investigated with human breast cancer MDA-MB-231 cells as a model cell line. The cellular uptake of **U-Ir@PAA-ABS** was first evaluated by confocal laser scanning microscopy (CLSM). Figure 3A,D shows that **U-Ir@PAA-ABS** is gradually internalized by MDA-MB-231 cells after incubation for 3 h and accumulates at 6–12 h. As shown in Figure 3B and Figure S26, the blue luminescence from the UCNPs irradiated at 980 nm overlaps well with the red luminescence from **Ir complex**, irradiated at 540–580 nm, suggesting that the UCNPs are not separated from the **Ir complex** after the NPs enter into the cells.

The subcellular distributions of **U-Ir@PAA-ABS** and **U-Ir@PAA** were also studied by co-staining experiments with MitoTracker Green. According to Figure 3C and S27 MDA-MB-231 cells were incubated with **U-Ir@PAA-ABS** or **U-Ir@PAA** for 6 h: the excellent superimposition between the MitoTracker Green and the NPs showed a high Pearson's correlation coefficient (PCC) of above 0.90, revealing selective accumulation of **U-Ir@PAA-ABS** and **U-Ir@PAA** in mitochondria due to the lipophilic moiety of **Ir complex**. Due to the short lifetime and limited diffusion distance of the ROS produced by PS during PDT, the sites of ROS generation directly influence their efficacy. Mitochondria are sensitive to ROS and are essential in regulating redox signaling and apoptosis pathways.[50] For these reasons, PSs targeting mitochondria could reduce the dosage, induce mitochondrial photodamage, and enhance the therapeutic effect.[28]

2.6 | The inhibition effects of U-Ir@PAA-ABS on CA IX

The inhibition effects of **U-Ir@PAA-ABS** on CA IX were studied at the cellular level. 4-Nitrophenyl acetate (4-NPA)
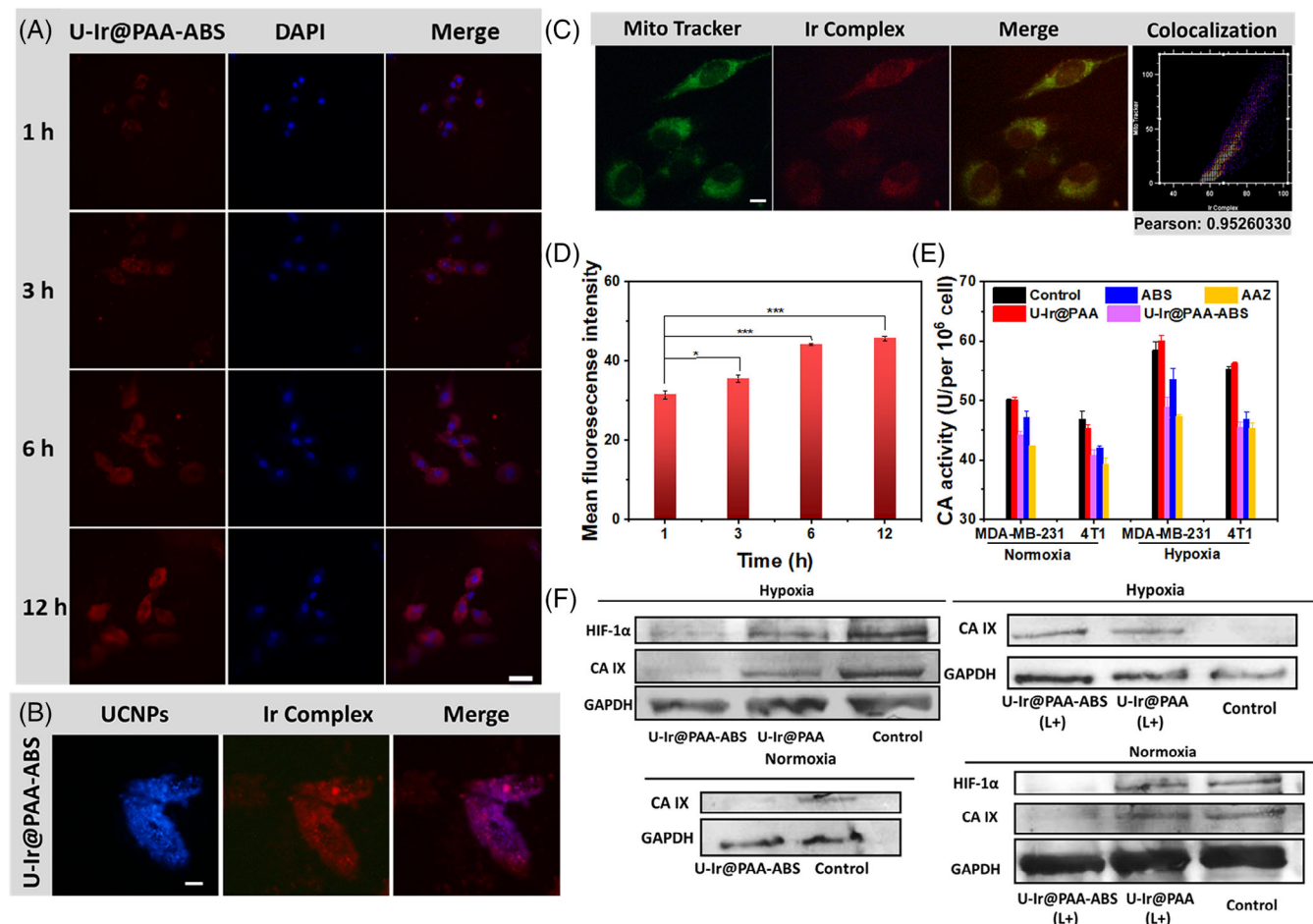
FIGURE 3 In vitro cellular investigation. (A) CLSM images of MDA-MB-231 cells after incubation with **U-Ir@PAA-ABS** (concentration of **Ir complex** = 20 μM) at different periods. Scale bar = 50 μm. (B) Colocalization assay of UCNPs and **Ir complex** in **U-Ir@PAA-ABS**. Scale bar = 10 μm. (C) Colocalization assay of **U-Ir@PAA-ABS** with MitoTracker Green in MDA-MB-231 cells. Scale bars = 10 μm. (D) Average fluorescence intensity of **U-Ir@PAA-ABS** after incubation with MDA-MB-231 cells at different times. Error bars, mean ± SD, $n = 3$, $*p < 0.05$, $***p < 0.001$. (E) Inhibitory activity of **U-Ir@ABS** and **U-Ir** against CA IX under different conditions. Acetazolamide (AAZ) (a commercial inhibitor of CA IX) and **ABS** were used as positive controls. (F) After different treatments, HIF-1α and CA IX expression in normoxic and hypoxic MDA-MB-231 cells using Western blot analysis.

was used as a substrate to test the CA IX enzymatic activity of MDA-MB-231 cells treated with different materials. As shown in Figure 3E the content of CA IX in the MDA-MB-231 cell culture increases significantly under hypoxia conditions, which is in accordance with a relatively higher CA IX expression level in hypoxic than in normoxic cancer cells.[45,51,52] Compared with the control group, the expression of CA IX in **U-Ir@PAA** treated cells showed almost no change. As expected, after incubation with **U-Ir@PAA-ABS** the activity of CA IX in cells was inhibited, and this effect is similar to that of acetazolamide (AAZ), which confirms that **U-Ir@PAA-ABS** has an excellent inhibitory effect on CA IX. The assembled **ABS** in **U-Ir@PAA-ABS** mainly blocks and suppresses the CA IX activity, similar to previous reports.[41,53] Compared with the other groups, a Western blot analysis indicates that **U-Ir@PAA-ABS** treatment significantly inhibits the expression of CA IX and HIF-1α in normoxia and hypoxic MDA-MB-231 cells (Figure 3F). These results show that **U-Ir@PAA-ABS** possesses CA IX binding and intervention ability, and alleviates tumor hypoxia to a certain extent, which would profit from the in situ generation of ROS and improvement of PDT efficacy.

2.7 | Intracellular photoinduced ROS generation ability of the nanoplatforms

The intracellular photoinduced ROS generation ability of **U-Ir@PAA-ABS** and **U-Ir@PAA** were investigated in MDA-MB-231 cells (Figure 4A–D). The total ROS level of cells treated with the NPs in normoxia and hypoxia conditions was monitored with 2′,7′-dichlorofluorescein diacetate (DCFH-DA) as a probe. Confocal imaging revealed negligible fluorescence in the control, with or without light irradiation, after treating cells with **U-Ir@PAA-ABS** and **U-Ir@PAA** in dark conditions. Enhanced green fluorescence was observed after 980 nm irradiation in normoxic cells, illustrating the excellent ROS generation ability of **U-Ir@PAA-ABS** and **U-Ir@PAA**. In hypoxic conditions, the NPs' ability for ROS generation was reduced to varying degrees. The green signal of **U-Ir@PAA-ABS** is brighter than that of **U-Ir@PAA** in hypoxic cells, meaning that **U-Ir@PAA-ABS** generates more ROS. Besides, there is no detectable signal in the UCNPs upon 980 nm laser irradiation, indicating the UCNPs have negligible ability to produce ROS (Figure S28). To better understand the mechanism of ROS generation, the ability of the NPs to produce type-II and
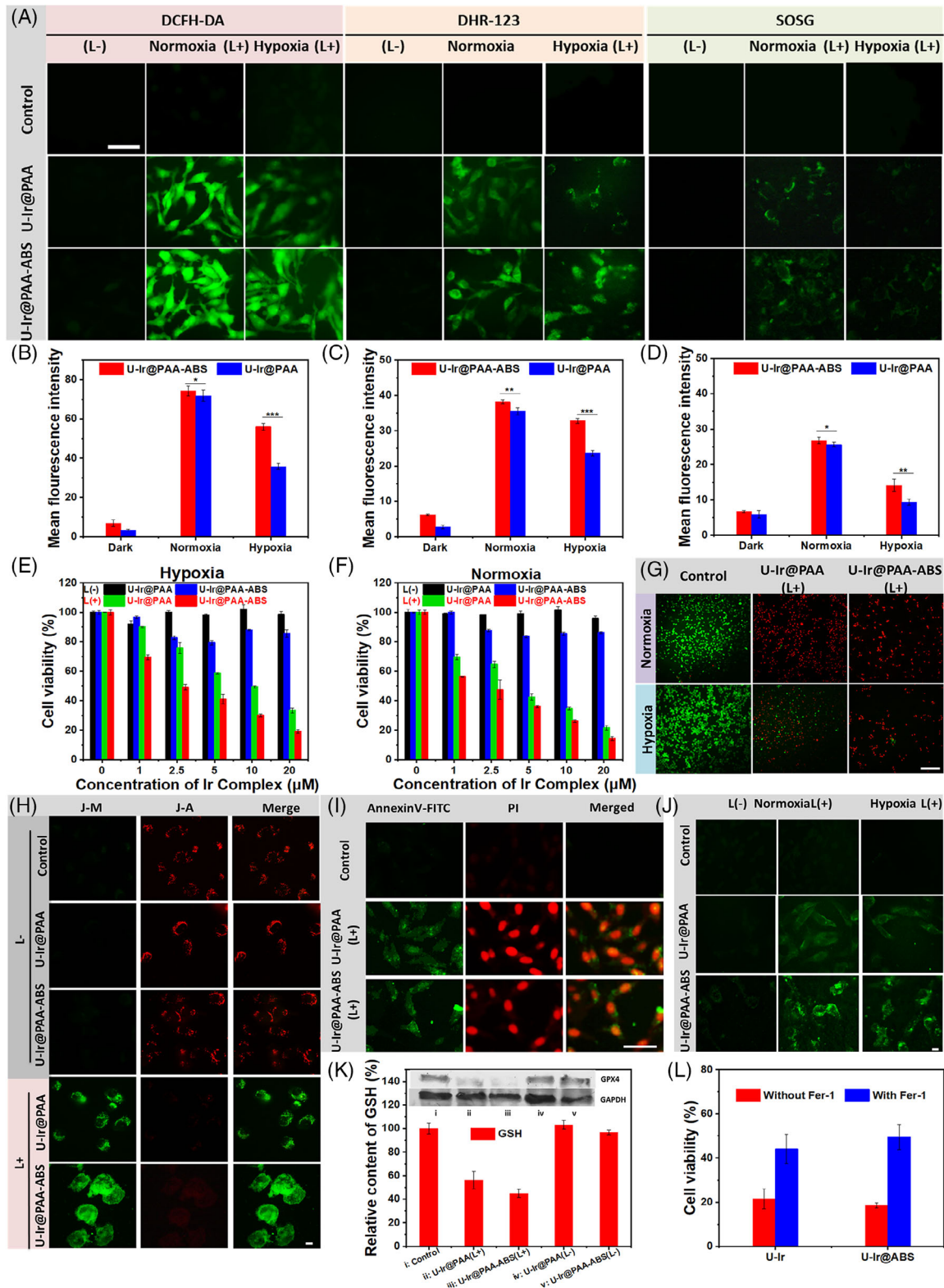
FIGURE 4 The intracellular ROS generation and cytotoxicity of **U-Ir@PAA-ABS** and the investigation of cell death mechanism. (A) Confocal fluorescence images for the detection of ROS: type-I ROS generation in MDA-MB-231 cells treated with **U-Ir@PAA** and **U-Ir@PAA-ABS** under irradiation (980 nm, 0.6 mW cm^{-2}) with different O_2 conditions. Scale bar = 50 μm. Average fluorescence intensity of DCFH (B), DHR123 (C) and SOSG (D) after MDA-MB-231 cells incubated with different nanoplantforms after irradiation (980 nm, 0.6 mW cm^{-2}). Error bars, mean ± SD, $n = 3$, *$p < 0.05$, **$p < 0.01$, ***$p < 0.001$. Relative viability of MDA-MB-231 cells after 24 h co-incubation with **U-Ir@PAA** and **U-Ir@PAA-ABS** under darkness and irradiation (980 nm, 0.6 mW cm^{-2}) in normoxic condition (E) and hypoxic condition (F). (G) Confocal fluorescence images of MDA-MB-231 cells co-stained with calcein-AM (live cells, green fluorescence) and PI (dead cells, red fluorescence) after treatment with **U-Ir@PAA-ABS** and **U-Ir@PAA** under darkness and under irradiation (980 nm, 0.6 mW cm^{-2}) at normoxic and hypoxic conditions. Scale bar = 100 μm. (H) Confocal fluorescence imaging of MMP in MDA-MB-231 cells incubated with **U-Ir@PAA** and **U-Ir@PAA-ABS** (darkness or 980 nm, 0.6 mW cm^{-2}) via subsequent JC-1 dye assay. Scale bar = 10 μm. (I) Death of MDA-MB-231 cells induced by **U-Ir@PAA-ABS** and **U-Ir@PAA** with irradiation (980 nm, 0.6 mW cm^{-2}) and staining with dual fluorescence of annexin V-FITC/PI. Scale bar = 50 μm. (J) Confocal fluorescence images for detecting the intracellular LPO level in MDA-MB-231 cells treated with **U-Ir** and **U-Ir@ABS** under irradiation (980 nm, 0.6 mW cm^{-2}) in different O_2 conditions. Scale bar = 10 μm. (K) Relative content of GSH in MDA-MB-231 cells after different treatments. Inset image: After different treatments, GPX4 expression in MDA-MB-231 cells from Western blot assays. (L) Relative viability of MDA-MB-231 cells after 24 h co-incubation with **U-Ir@PAA-ABS** and **U-Ir@PAA** under irradiation (980 nm, 0.6 mW cm^{-2}) with or without ferrostatin-1.

type-I ROS was tested separately. The fluorescent sensor singlet oxygen sensor green (SOSG) was used as an indicator for $^1O_2$ detection. **U-Ir@PAA-ABS** and **U-Ir@PAA** produced $^1O_2$ in normoxic cells irradiated with 980 nm light, demonstrating the type-II mechanism of PDT in the NPs. CLSM was performed using DHR 123 to stain cells treated with **U-Ir@PAA-ABS** and **U-Ir@PAA**. Similar to the total ROS test results, the NPs alone hardly triggered the fluorescence of the indicator under dark conditions, but the green fluorescence was significantly enhanced after exposure to a laser, illustrating that **U-Ir@PAA-ABS** and **U-Ir@PAA** produce type-I ROS in cells. Besides, the green fluorescence in **U-Ir@PAA** treated cells was dramatically decreased in hypoxia conditions compared with **U-Ir@PAA-ABS** treatment, which indicates that **U-Ir@PAA-ABS** is more effective in type-I photochemical reaction processes. In general, as the mechanism of chemical changes in photooxidations for the formation of type-I ROS, the main source of $O_2^{-\bullet}$ in photosensitized reactions could be obtained by the PSs' radical anion reacting with O_2 to regenerate the sensitizer and to form $O_2^{-\bullet}$, which is much more relevant than the direct reduction of O_2.[54] In some cases, O_2 is needed in the overall photochemical process to prevent the recovery of the substrate via quenching PS^{-}[54]. Owing to the reduced HIF-1α expression level by **U-Ir@PAA-ABS** in MDA-MB-231 cells, the **U-Ir@PAA-ABS** treated group showed better anti-hypoxia ability, and then the type-I photochemical process was facilitated to produce more $O_2^{-\bullet}$. The above results demonstrate that **U-Ir@PAA-ABS** leads to enhanced type-I ROS generation upon 980 nm irradiation with low oxygen dependence which is favorable for killing cancer cells and boosting PDT efficacy.

## 2.8 | Cytotoxicity of nanoplatforms against MDA-MB-231 cells

The viability of MDA-MB-231 cells was evaluated under various conditions in vitro, as shown in Figure 4E,F. The MDA-MB-231 cells were incubated with no treatment, **U-Ir@PAA** or **U-Ir@PAA-ABS** at different concentrations, followed by no treatment or by laser exposure in normoxia or hypoxia conditions. The results indicate obvious cytotoxicity when MDA-MB-321 cells were treated with **U-Ir@PAA-ABS** and **U-Ir@PAA** upon 980 nm laser irradiation in normoxia conditions (**U-Ir@PAA-ABS**: IC$_{50}$ value = 1.79 μM, **U-Ir@PAA**: IC$_{50}$ value = 3.88 μM in normoxia). In addition, the photo-cytotoxicity of **U-Ir@PAA-ABS** to MDA-MB-231 cells in 1% O_2 conditions is similar to that of incubation in normoxia (**U-Ir@PAA-ABS**: IC$_{50}$ value = 2.60 μM, **U-Ir@PAA**: IC$_{50}$ value = 8.73 μM in hypoxia). As shown in live-dead cell staining experiments (Figure 4G and Figure S29), **U-Ir@PAA-ABS** and **U-Ir@PAA** demonstrate negligible red fluorescence in dark conditions. Even hypoxic cells incubated with **U-Ir@PAA** still have red fluorescence after 980 nm irradiation, suggesting the cell phototoxicity of **U-Ir@PAA**, confirming that it could inhibit hypoxic cancer cells. Almost no green fluorescence was observed in cells treated with **U-Ir@PAA-ABS** under 980 nm irradiation, whether in normoxia or hypoxia conditions. These results demonstrate that **U-Ir@PAA-ABS** causes an excellent phototoxic effect upon 980 nm irradia-

tion in the case of hypoxic MDA-MB-231 cell lines and can effectively attenuate the limitation of tumor hypoxia on PDT efficiency.

2.9 | The investigation of cell death mechanism

To investigate the detailed mechanism of this mitochondria-targeted type-I PDT, the cell death modes were assessed. Apoptosis is the most common cell death pathway during PDT treatment.[6] Once the mitochondria are photodamaged, they lose membrane potential and stimulate apoptosis.[50] The loss of mitochondrial membrane potential (MMP) is detected by a JC-1 assay. MDA-MB-231 cells showed only intensive red fluorescence in the control and darkness groups, indicating high MMP values (Figure 4H). Conversely, both **U-Ir@PAA-ABS** and **U-Ir@PAA** induced the MMP to drop upon 980 nm irradiation, reflecting mitochondrial dysfunction which is consistent with the cytotoxicity assay. The photo-cytotoxicity of **U-Ir@PAA-ABS** and **U-Ir@PAA** against MDA-MB-231 cells was further investigated by detecting the dual fluorescence of annexin V-FITC/propidium iodide (PI) with confocal microscopy. Annexin V-FITC emits green fluorescence, while PI gives red fluorescence. As shown in Figure 4I, the control group exhibited no observable fluorescence of annexin V-FITC/PI, while the **U-Ir@PAA-ABS** and **U-Ir@PAA** treated cells after irradiation displayed intense green and red fluorescence, showing apoptotic characteristics, suggesting they underwent cell death via apoptosis.

The stimulation of ROS within mitochondria could also exhaust the cellular free radical scavenger reduced glutathione (GSH).[5] As shown in Figure 4K, upon irradiating **U-Ir@PAA-ABS**-prestained MDA-MB-231 cells with a 980 nm laser (0.6 mW cm^{-2}, 10 min), the level of intracellular GSH reduced significantly compared with the initial value, confirming the excellent GSH depletion ability of **U-Ir@PAA-ABS**. GSH depletion can induce the accumulation of lipid peroxidase (LPO) and deactivate the metabolism of glutathione peroxidase 4 (GPX4) and ultimately facilitate ferroptosis.[55] To detect the accumulation of LPO inside cells treated with **U-Ir@PAA-ABS**, Liperfluo was used as a specific LPO probe. NPs enhanced the probe's fluorescence remarkably via photoirradiation (Figure 4J), indicating the obvious accumulation of LPO. As depicted in Figure 4L, the ferroptosis inhibitor (ferrostatin-1, Fer-1) led to a notable viability enhancement of NP-treated cells, implying ferroptosis might be another cell death pathway induced by the NPs upon 980 nm irradiation. To understand the accumulation of LPO in hypoxic cells, Tiron (disodium 4,5-dihydroxy-1,3-benzenedisulfonate) was used as a superoxide scavenger to inhibit O_2^{-} (Figure S30), inducing a visible drop in LPO accumulation; these results are consistent with a previous report.[56] It is validated that the ferroptosis of NP-treated hypoxic cells could be attributed to a type-I photochemical process of **U-Ir@PAA-ABS**. On the other hand, a Western blot assay demonstrated that the irradiated **U-Ir@PAA-ABS** inhibited the expression of the LPO scavenger GPX4, which would also cause LPO accumulation and eventually ferroptosis (Figure 4K). Notably, this mechanism is a new
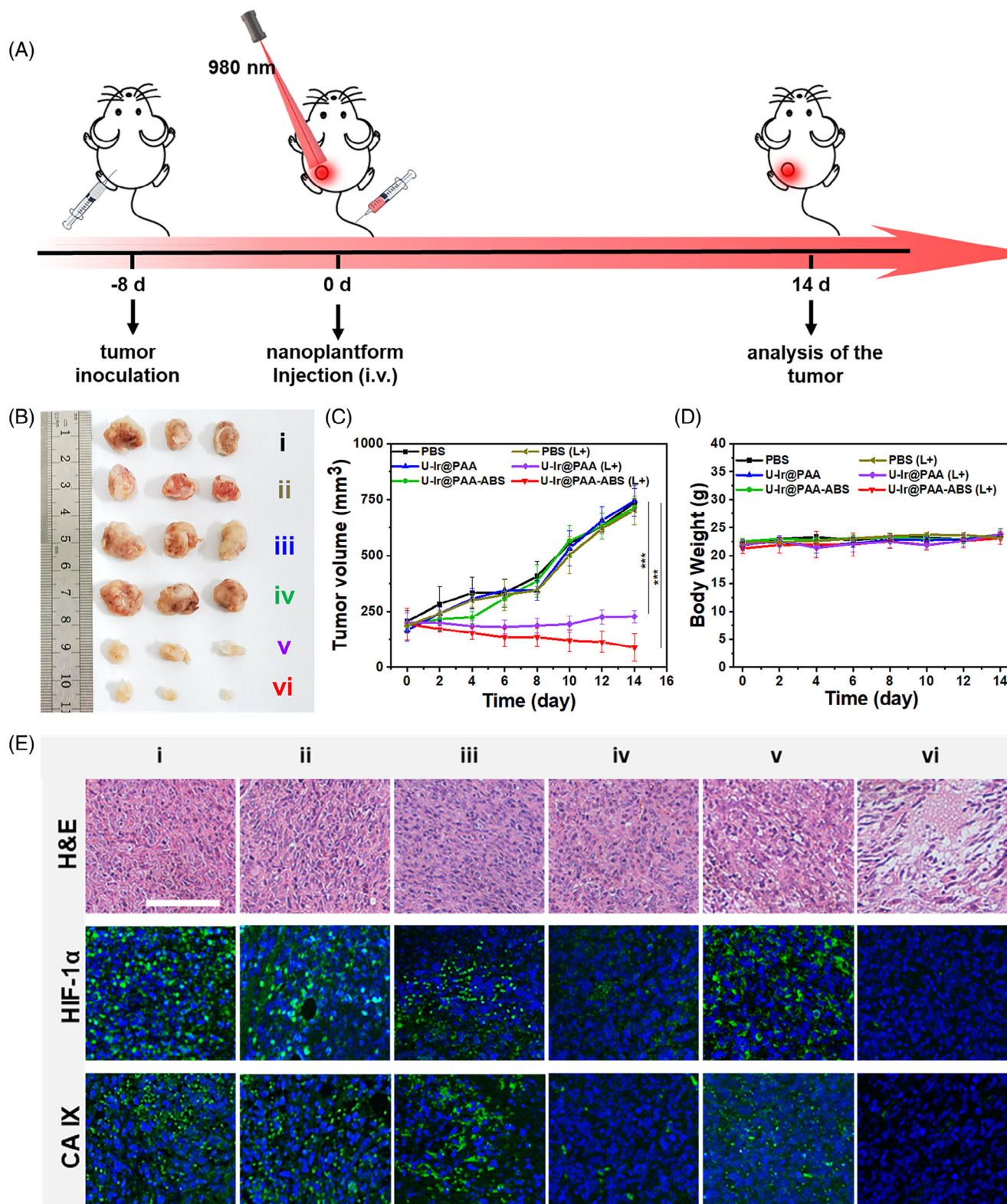
FIGURE 5 **U-Ir@PAA-ABS** and **U-Ir@PAA-**mediated inhibition of tumor growth in **4T1** tumor model. (A) Timeline of the treatment. (B) Photos of tumors after treatment. (C) Relative tumor volume in different groups, ***$p < 0.001$. (D) Changes in the body weights of mice. (E) H&E staining images and immunofluorescence analysis of tumor tissues from the different groups on day 14; scale bar: 100 μm.

form of non-apoptotic programmed cell death for tumor suppression, avoiding the occurrence of drug resistance.[57] The suppression of the CA IX level could acidify the intracellular pH and cause susceptibility to alterations in iron homeostasis.[53,58] Moreover, inhibiting HIF-1α was a feasible strategy for restraining ferroptosis resistance in hypoxia solid tumors.[59] Overall, **U-Ir@PAA-ABS** achieves an outstanding multifunctional ferroptosis photoinduction. All the results establish that **U-Ir@PAA-ABS** induces cell death by apoptosis and ferroptosis under 980 nm irradiation and its ability to alleviate hypoxia further raises the photoirradiation therapeutic efficacy.

2.10 | In vivo PDT investigation of nanoplatforms

Inspired by the excellent in vitro antitumor efficiency of **U-Ir@PAA-ABS**, its in vivo therapy was studied in mice bearing homogenotypic 4T1 tumors. A Cell Counting Kit-8 (CCK-8) assay showed that the phototoxicity of **U-Ir@PAA-ABS** against hypoxic 4T1 cells under 980 nm irradiation gave an IC_{50} value of 5.80 μM (Figure S31). The 4-NPA assay also indicates the inhibition effects of **U-Ir@PAA-ABS** on CA IX in 4T1 cells (Figure 3E). The murine models were established by injecting 4T1 cells into the left thigh subcutaneously (Figure 5A). The tumor-bearing mice were then randomly divided into six groups and were intravenously injected with phosphate buffered saline (PBS) (group i); with PBS and laser irradiation (980 nm, 0.6 W cm^{-2}, 10 min) (ii); with **U-Ir@PAA** (40 μM of **Ir complex**, 200 μL) (iii); with **U-Ir@PAA-ABS** (40 μM of **Ir complex**, 200 μL) (iv); with **U-Ir@PAA** and laser (v); and with **U-Ir@PAA-ABS** and laser (vi). According to the Yb content in inductively coupled plasma mass spectrometry (ICP-MS) experiments (Figure S33), **U-Ir@PAA-ABS** accumulated in tumor tissues in 8–24 h and subsequently gradually decreased during 48–72 h. The changes in the tumor volume and the body weight of each mouse were recorded during 14 days. As shown in Figure 5B,C, and Figure S32 in groups (i), (ii), (iii) and (iv), the relative tumor volumes increased about 4 times after 14 days. In comparison, the significantly reduced tumor volumes in groups (v) and (vi) indicate the good antitumor activity of **U-Ir@PAA** and **U-Ir@PAA-ABS** upon 980 nm irradiation; and the irradiated **U-Ir@PAA-ABS** has a more excellent therapeutic effect due to the load of ABS. The accumulation of **U-Ir@PAA-ABS** in main organs and collected feces at different times was tested by determination of Yb content using ICP-MS (Figures S34 and S35), which indicated that the **U-Ir@PAA-ABS** excreted more through feces in the first 8 h, and **U-Ir@PAA-ABS** mainly accumulates in the liver, spleen and kidney within 8–24 h and gradually decreases after 72 h.

After 14 days of treatment, the mice were sacrificed, and the tumors, as well as the subject organs (heart, liver, spleen, lung and kidneys) were excised for histological analysis. As shown from the Hematoxylin and Eosin (H&E) staining (Figure 5E), there are many stromal tight cells, and the nucleus and cytoplasm were intact in the control group, indicating the good condition of the cells. The tissue space presented hiatus and the tumor cells were destroyed in the **U-Ir@PAA-ABS (L+)** group. As expected, the tumor proliferation was significantly inhibited by **U-Ir@PAA-ABS** + 980 nm treatment. Furthermore, immunofluorescence staining showed that both CA IX and HIF-1α overexpress in groups (i), (ii), (iii) and (v), but **U-Ir@PAA-ABS** treatment notably weakened the signals of CA IX and HIF-1α, indicating the success of alleviating hypoxia inside the solid tumor (Figure 5E). There were no obvious body weight losses in the groups (Figure 5D) and negligible pathological changes were observed in the main organs from the six groups (Figure S36), suggesting that **U-Ir@PAA-ABS** is not toxic to normal tissues. The above results reveal that **U-Ir@PAA-ABS** effectively inhibits tumor growth under 980 nm irradiation, indicating its potential application in treatment of deep-tissue cancer.

3 | CONCLUSION

In summary, we have designed a next-generation multifunctional NIR-triggered nanophotosensitizer, **U-Ir@PAA-ABS**, with the ability to target mitochondria, to produce type-I and type-II ROS in aggregates and to alleviate hypoxic tumors. The rationally designed AIE-active **Ir complex**-PSs exhibited efficient type-I and type-II ROS generation either alone or coupled to **UCNPs** upon 980 nm excitation. **U-Ir@PAA-ABS** has reasonable stability in water and outstanding photostability. In vitro experiments demonstrate that **U-Ir@PAA-ABS** is taken up efficiently by MDA-MB-231 cells, targets mitochondria, generates type-I and type-II ROS, reduces GSH and performs excellent cytotoxicity on hypoxic cells via photoirradiation at the cellular level. Further analysis of the cell death mechanism found that **U-Ir@PAA-ABS** has anticancer activity through two modes: (i) apoptosis, usually induced by PDT, and (ii) ferroptosis, caused by accumulated LPO. The inhibition of **U-Ir@PAA-ABS** on CA IX and HIF-1α expression not only assists hypoxia alleviation and further promotes the generation of type-I ROS in hypoxic cells but also suppresses ferroptosis resistance; the multi-effect mechanism confirms that **U-Ir@PAA-ABS** has unique potential for photoirradiation cancer treatment. In vivo results prove that **U-Ir@PAA-ABS** can effectively inhibit tumor growth under 980 nm irradiation without significantly damaging normal tissues. Overall, this work establishes a new and highly efficient "three birds with one stone" method for constructing NIR-irradiation PSs with hypoxia alleviation and offers great promise for deep-tissue tumor therapy.

4 | EXPERIMENTAL SECTION

4.1 | Materials and instruments

Materials for organic synthesis were purchased from Energy Chemical Company. Indocyanine green (ICG), 5,5-dimethyl-1-pyrroline-*N*-oxide (DMPO), 2,2,6,6-tetramethylpiperidine (TEMP) and dihydrorhodamine 123 (DHR 123) were purchased from Energy Chemical Company. RPMI Medium 1640 was purchased from Solarbio Life Science Company. Fetal bovine serum (FBS) was purchased from Sigma-Aldrich. Cell Counting Kit-8 (CCK-8), 2′7′-dichlorodihydrofluorescein diacetate (DCFH-DA) and the cell viability (live dead cell staining) assay kit were purchased from Shanghai Beyotime Biotechnology Co., Ltd. ^{1}H NMR spectra were recorded at 25°C on a Varian 500 MHz spectrometer. UV–vis absorption spectra were recorded on a Shimadzu UV-3100 spectrophotometer. The photoluminescence spectra, excited state lifetimes (τ) and photoluminescence quantum yields (Φ) were recorded on an Edinburgh FLS920 spectrofluorimeter under air at room temperature. Transmission electron microscopy (TEM) images were taken by a JEM-2100 PLUS Electron Microscope. Diameter and diameter distribution of the nanoparticles were determined by a Malvern Zetasizer Nano instrument for dynamic light scattering (DLS). Confocal laser scanning microscopy (CLSM) images were taken using a ZeissLSM 700 instrument (Zurich, Switzerland). Inductively coupled

plasma mass spectrometry (ICP-MS) used a PerkinElmer NexION 300D ICP-MS instrument (PerkinElmer, USA).

4.2 | Synthesis of [(ppy-COOCH$_3$)$_2$Ir-(L)-Ir(ppy-COOCH$_3$)$_2$][PF$_6$]$_2$(C)

An orange suspension of the dichloro-bridged diiridium complex [Ir(ppy-COOCH$_3$)$_2$Cl]$_2$ (1.304 g, 1 mmol) and Schiff base bridging ligand L (362 mg, 1 mmol) in MeOH (30 mL) and CH$_2$Cl$_2$ (30 mL) was refluxed under an inert atmosphere of N$_2$ in the dark for 8 h. The red solution was then cooled to room temperature, and solid ammonium hexafluorophosphate (0.37 g, 20 mmol) was added to the solution. The mixture was stirred for 30 min at room temperature and the suspension was then filtered and the precipitate was washed with petroleum ether and dried. The crude product was recrystallized from petroleum ether to yield C as a red solid. The product was purified by silica gel column chromatography with CH$_2$Cl$_2$/MeOH (200:1-50:1 v/v) as eluent. Yield: 65%. ^{1}H NMR (500 MHz, DMSO-d_6 δ [ppm]): 9.61 (s, 1H), 8.55 (dd, J = 15.1, 6.7 Hz, 2H), 8.46 (d, J = 8.3 Hz, 1H), 8.33 (t, J = 7.7 Hz, 1H), 8.24 (d, J = 8.2 Hz, 1H), 8.14 (t, J = 7.7 Hz, 1H), 8.09 (t, J = 6.6 Hz, 2H), 7.83 (d, J = 5.2 Hz, 1H), 7.75 (dd, J = 13.4, 7.0 Hz, 3H), 7.60 (d, J = 8.1 Hz, 1H), 7.46 (d, J = 4.6 Hz, 1H), 7.41 (t, J = 6.6 Hz, 1H), 7.37 (ddd, J = 8.1, 3.6, 1.5 Hz, 1H), 7.32 (dd, J = 15.8, 8.6 Hz, 2H), 6.95 (dd, J = 12.7, 8.6 Hz, 2H), 6.70 (s, 1H), 6.65 (dd, J = 5.1, 1.4 Hz, 1H), 3.66 (d, J = 8.0 Hz, 6H) (Figure S3).

4.3 | Synthesis of [(ppy-COOH)$_2$Ir-(L)-Ir(ppy-COOH)$_2$][PF$_6$]$_2$ (Ir complex)

The obtained complex C was dissolved in 10 mL of THF/MeOH (5:1). A saturated solution of LiOH was added slowly with constant stirring until pH = 8–9. The reaction mixture was stirred at 60°C for 36 h. After completion of the reaction, the solvent was removed under reduced pressure and the resulting residue was suspended in a mixture of water and CH$_2$Cl$_2$. The aqueous layer was separated and concentrated using a rotary evaporator to remove any traces of CH$_2$Cl$_2$. HCl 10% was added dropwise until pH = 1–2. The red solution was then filtered and the filtrate was suspended to obtain a red solid. The product was washed with water and dried at 68°C to give [(ppy-COOH)$_2$Ir-(L)-Ir(ppy-COOH)$_2$][PF$_6$]$_2$ (Ir complex). Yield: 50%. ^{1}H NMR (500 MHz, DMSO-d_6 δ [ppm]): 13.03–12.21 (s, 2H), 9.72 (s, 1H), 8.60 (s, 1H), 8.56 (s, 1H), 8.44 (d, J = 7.6 Hz, 1H), 8.32 (s, 1H), 8.22 (d, J = 7.5 Hz, 1H), 8.12–8.05 (m, 3H), 7.80 (d, J = 4.8 Hz, 1H), 7.74 (dd, J = 16.4, 10.0 Hz, 3H), 7.58 (d, J = 8.0 Hz, 1H), 7.44–7.40 (m, 1H), 7.38 (m, 1H), 7.35 (d, J = 8.1 Hz, 1H), 7.29 (d, J = 8.8 Hz, 2H), 6.93 (t, J = 13.1 Hz, 2H), 6.71 (s, 1H), 6.66 (d, J = 6.2 Hz, 1H) (Figure S4). MS (MALDI-TOF) [m/z]: 770.1597 (M^{2+}) (Figure S5). Calcd. for C$_{72}$H$_{50}$F$_{12}$Ir$_2$N$_8$O$_8$P$_2$: C 47.27, H, 2.75, N 6.12. Found C 47.44, H 2.68, N 6.14.

4.4 | Preparation of U-Ir@PAA and U-Ir@PAA-ABS

The prepared UCNPs were stirred with HCl to remove OA and centrifuged to remove the supernatant. The collected NPs were dispersed in DMF and stirred with PAH for 6 h, then centrifuged to remove the supernatant to collect U-PAH. The U-PAH was dispersed in 2 mL DMSO. 2 mL of 1.5 mg mL^{-1} Ir complex in DMSO, 2 mg EDCl and 2 mg NHS were stirred for 1 h and then 1 mL U-PAH was added, and the mixture was stirred overnight. Next, the mixture was centrifuged at 12,000 rpm for 15 min to remove the supernatant and washed with DMSO three times to form U-Ir. The collected U-Ir was dispersed in 1 mL water. The polyacrylic acid (PAA) was dissolved in DMF and stirred with the same eq. of EDCl, NHS and 4-(2-aminoethyl)benzenesulfonamide (ABS) overnight. The product was dialyzed (3500 kD) in water to obtain PAA-ABS. 300 μL U-Ir was slowly dropped into 20 μg mL^{-1} PAA or PAA-ABS during high-speed stirring, and then the mixture was stirred for 4 h. Next, the mixture was centrifuged at 11,000 rpm for 8 min and washed with water twice, then dispersed in 1 mL water to form U-Ir@PAA and U-Ir@PAA-ABS. The weight percent of the Ir complex in U-Ir@PAA and U-Ir@PAA-ABS was calculated with standard curve data (Figure S7).

4.5 | Test method for ROS generation in solution

4.5.1 | ROS, O$_2^{-\bullet}$ and •OH generation test with DCFH, DHR 123 and HPF

Ir complex was mixed with indicator solutions as working solutions, and then was illuminated with 405 nm LED at 20 mW cm^{-2} for 180 s. For 99%: Ir complex 10 μM in mixed solvent (MeOH/H$_2$O = 1/99), and for 0%: Ir complex 10 μM in MeOH. The nanoplatforms were mixed with indicator solution as working solutions, and then illuminated with 980 nm laser at 0.6 W cm^{-2} for 30 min.

4.5.2 | ^{1}O$_2$ generation test with ICG

Ir complex was mixed with ICG solution as working solutions, and then was illuminated with 405 nm LED at 20 mW cm^{-2} for 180 s. For 99%: Ir complex 10 μM in mixed solvent (MeOH/H$_2$O = 1/99), and for 0%: Ir complex 10 μM in MeOH. U-Ir was mixed with ICG solution as working solutions, and then was illuminated with 980 nm laser at 0.6 W cm^{-2} for 30 min.

4.5.3 | ^{1}O$_2$ generation test with ABDA

Nanoplatforms were mixed with ICG solution as working solutions, and then were illuminated with a 980 nm laser at 0.6 W cm^{-2} for 30 min.

4.5.4 | $^1O_2$ generation test with TEMP

EPR analysis was performed using TEMP as a spin-trap agent. 10 μL of TEMP was added to 20 μM **Ir complex**, 300 μg mL^{-1} **U-Ir@PAA** or **U-Ir@PAA-ABS**. The spectra were monitored in a range of 3360–3480 G after the solution was irradiated by 405 nm LED at 20 mW cm^{-2} or 980 nm 0.6 W cm^{-2} for 5 min.

4.5.5 | $O_2^{-\bullet}$ generation test with DMPO

EPR analysis was performed using DMPO as a spin-trap agent. MeOH solution containing 20 mM DMPO (30 μL) was added to 20 μM **Ir complex**, 300 μg mL^{-1} **U-Ir@PAA** or **U-Ir@PAA-ABS**. The spectra were monitored in a range of 3340–3500 G after the solution was irradiated by 405 nm LED at 20 mW cm^{-2} or 980 nm 0.6 W cm^{-2} for 5 min.

4.6 | Cell culture

MDA-MB-231 cells and 4T1 cells were cultured. The culture medium was prepared by RPMI Medium 1640 containing 10% (v:v) FBS. The cell culture flask was placed in the incubator at normoxia condition: cells were maintained in a humidified atmosphere containing 5% CO_2 at 37°C. Hypoxic condition: cells was maintained at 37°C in a humidified atmosphere containing 1% O_2, 5% CO_2, 94% N_2.

4.7 | Cytotoxicity test method

The cytotoxicity of **U-Ir@PAA** and **U-Ir@PAA-ABS** was detected by CCK-8 assay. MDA-MB-231 or 4T1 cells were seeded in 96-well plates at a density of 10,000 cells per well. The cells were cultured in the incubator at normoxia or hypoxia conditions for 24 h. After aspirating the old culture medium, 100 μL RPMI Medium 1640 containing different concentration gradient PSs (0–20 μM of **Ir complex**) were added to each well. The original culture medium was replaced by 100 μL fresh RPMI Medium 1640 after 6 h. The light group was irradiated with a 980 nm laser at 0.6 W cm^{-2} for 2 min, 5 times, while the dark group was not illuminated. After irradiation, the cells were placed in the incubator for 24 h. The absorbance value of the sample at 450 nm was detected by a microplate reader. Then CCK-8 (10 μL) was added to each well. The cells were placed in the incubator for 1 h. The absorbance value at 450 nm was detected, and then the cell viability was calculated after subtracting the two test results.

4.8 | Intracellular localization measurements

Cells were incubated with **U-Ir@PAA** and **U-Ir@PAA-ABS** (5 μM) for 6 h, and then stained with MitoTracker Green (200 nM) for another 30 min. The cells were then washed twice with PBS, and fresh medium was replenished before visualization by CLSM. $\lambda_{ex} = 540$–580 nm, $\lambda_{em} = 600$–660 nm for nanoplantforms and $\lambda_{ex} = 465$–495 nm, $\lambda_{em} = 415$–555 nm for MitoTracker Green.

4.9 | Evaluation of intracellular ROS production capacity

MDA-MB-231 cells were seeded in confocal dishes at a density of 50,000 cells per well and incubated in normoxia and hypoxia conditions for 24 h. The original medium was aspirated and RPMI Medium 1640 (1 mL) containing **U-Ir@PAA** and **U-Ir@PAA-ABS** (10 μM) was added to the dish. After continuing to culture in the incubator for 6 h, the supernatant was removed and 1 mL RPMI 1640 was added. The illumination group was irradiated with a 980 nm laser (0.6 W cm^{-2}) for 2 min, 3 times, and the dark group was treated with the same treatment without illumination. After light exposure, the original medium was aspirated and washed with PBS. For a total ROS level test, the cells were stained with DCFH-DA and imaged by CLSM. Similar methods were used for $^1O_2$ and $O_2^{-\bullet}$ tests, with different indicators, SOSG and DHR-123 to observe the green fluorescence intensity in the cells. $\lambda_{ex} = 465$–495 nm, $\lambda_{em} = 415$–555 nm for indicators.

4.10 | Intracellular LPO detection in normoxic MDA-MB-231 cells

The intracellular LPO levels were measured by Liperfluo. MDA-MB-231 cells were seeded in confocal dishes at the density of 50,000 cells per well and incubated in normoxia and hypoxia conditions, respectively, for 24 h. The cells were incubated with **U-Ir@PAA** and **U-Ir@PAA-ABS** (10 μM) at the indicated concentrations for 6 h in the dark, and then irradiated with a 980 nm laser at 0.6 W cm^{-2} for 2 min, 5 times. The cells were then washed with sterile PBS. the cells were stained with Liperfluo (1 μL), followed by CLSM to observe the green fluorescence intensity in the cells. $\lambda_{ex} = 465$–495 nm, $\lambda_{em} = 415$–555 nm for Liperfluo.

4.11 | Intracellular GSH and CA IX measurement

Cells (2×10^5/well) were cultured in a six-well plate and treated with different formulations (Control, **U-Ir@PAA (L-)**, **U-Ir@PAA-ABS (L-)**, **U-Ir@PAA (L+)** and **U-Ir@PAA-ABS (L+)**). The GSH amount was measured using a GSH assay kit; the CA IX amount was measured using a CA IX assay kit.

4.12 | Detection of mitochondrial membrane potential

The MDA-MB-231 cells were incubated in a glass-bottom dish at a density of 50,000 cells/dish for 24 h, and then the cells were subjected to different treatments (Control, **U-Ir@PAA (L-)**, **U-Ir@PAA-ABS (L-)**, **U-Ir@PAA (L+)** and **U-Ir@PAA-ABS (L+)**). Next, the cells were incubated

with JC-1 (5 μg mL^{-1}) at 37°C for 20 min. Then, the cells were washed with PBS. After that, the cells were imaged by CLSM.

4.13 | Western blotting

Western blotting was measured according to the manufacturer's protocols with slight modification. GAPDH antibody was used as the loading control. For GAPDH, CA IX, HIF-1α and GPX-4 expression, the cells were incubated with different treatments. MDA-MB-231 Cells (2×10^5/well) were cultured in a six-well plate and treated with different formulations (Control, **U-Ir@PAA (L-)**, **U-Ir@PAA-ABS (L-)**, **U-Ir@PAA (L+)** and **U-Ir@PAA-ABS (L+)**) The cells were then collected for evaluation via Western blotting. $\lambda_{ex} = 540$–580 nm, $\lambda_{em} = 600$–660 nm for J-A and $\lambda_{ex} = 465$–495 nm, $\lambda_{em} = 415$–555 nm for J-M.

4.14 | Annexin V-FTIC/PI assays

MDA-MB-231 cells were seeded in confocal dishes at a density of 50,000 cells per well. Different formulations (Control, **U-Ir@PAA (L+)**, **U-Ir@PAA-ABS (L+)**) were added to the medium and the cells were incubated for another 6 h. Then the cells were irradiated with a 980 nm laser at 0.6 W cm^{-2} for 2 min, 5 times, and further incubated in the dark for 24 h. Finally, the cells were stained with Annexin-FITC/PI for 15 min and then were imaged by CLSM. $\lambda_{ex} = 540$–580 nm, $\lambda_{em} = 600$–660 nm for PI and $\lambda_{ex} = 465$–495 nm, $\lambda_{em} = 415$–555 nm for Annexin V-FTIC.

4.15 | Animals and tumor model

The mice experiments were performed in accordance with animal regulations and management protocols. All animal experiments were approved by Institutional Animal Care and Use Committee of Northeast Normal University. BALB/c mice (female, 6–8 weeks) were purchased from Vital River Company in Beijing. 4T1 cells (1.0×10^6/tumor, 100 μL in PBS) were subcutaneously injected into the left flank of each mouse to establish the 4T1 tumor model.

4.16 | Evaluation of antitumor efficacy in vivo

When the tumor volume grew to about 150–200 mm^3 the mice were randomly separated into six groups. Then the mice were injected with PBS (i); with PBS and laser (980 nm, 0.6 W cm^{-2}, 10 min) (ii); with **U-Ir@PAA** (40 μM of **Ir complex**, 200 μL) (iii); with **U-Ir@PAA-ABS** (40 μM of **Ir complex**, 200 μL) (iv); with **U-Ir@PAA** and laser (v); and with **U-Ir@PAA-ABS** and laser (vi). The tumor sizes and body weights of the mice were monitored every two days during the 14 days of treatment. The tumor volume was measured as volume = ($L \times W^2$/2), where L (length) and W (width) are two tumor dimensions, respectively. On day 14, the mice in each group were euthanized, and the tumors and major organs were harvested for subsequent analysis. The tissues were fixed with formalin and then paraffin-embedded. The paraffin-embedded tissues were sectioned and stained with H&E to determine tissue damage after observation under a microscope.

4.17 | Immunofluorescence analysis

The paraffin-embedded tissues of the tumors were washed with dimethylbenzene (mixture of three isomers) and dehydrated in ethanol. The tumor sections were hydrated in 1× PBS for 5 min. The sections were incubated in 10 mM sodium citrate buffer for antigen retrieval (pH = 6.0, 90°C, 10 min). The sections were cooled to room temperature, washed twice with PBS for 5 min, and incubated in PBS containing 3% hydrogen peroxide for 5 min to block endogenous peroxidases. The sections were washed twice with PBS for 5 min and then treated with 0.1% Triton X-100 (PBS) for 45 min. Subsequently, the sections were incubated with 2% BSA for another 1 h. The sections were then incubated with CA IX, and HIF-1α primary antibodies overnight at 4°C. After PBS washing, the sections were incubated with Alexa Fluor 488-labeled secondary antibody for 1 h at room temperature. After DAPI staining, the cells were observed by CLSM.

4.18 | Statistical analysis

All analytical data were expressed as mean ± SD. $n \geq 3$ for all in vitro and in vivo experiments. The data were classified according to the p-values and denoted by (*) for $p < 0.05$, (**) for $p < 0.01$, and (***) for $p < 0.001$.

CONFLICT OF INTEREST STATEMENT
The authors declare no conflicts of interest.

DATA AVAILABILITY STATEMENT
The data that support the findings of this study can be found in the Supporting Information or are available from the corresponding author upon reasonable request.

ORCID
Martin R. Bryce https://orcid.org/0000-0003-2097-7823

REFERENCES
1. I. J. MacDonald, T. J. Dougherty, *J. Porphyrins Phthalocyanines* **2001**, *05*, 105.
2. Y. Wan, L.-H. Fu, C. Li, J. Lin, P. Huang, *Adv. Mater.* **2021**, *33*, 2103978.
3. Z. Zhou, J. Song, L. Nie, X. Chen, *Chem. Soc. Rev.* **2016**, *45*, 6597.
4. X. Kang, Y. Zhang, J. Song, L. Wang, W. Li, J. Qi, B. Z. Tang, *Nat. Commun.* **2023**, *14*, 5216.

5. J. Zhuang, B. Wang, H. Chen, K. Zhang, N. Li, N. Zhao, B. Z. Tang, *ACS Nano* **2023**, *17*, 9110.

6. F. Wei, J. Karges, J. Shen, L. Xie, K. Xiong, X. Zhang, L. Ji, H. Chao, *Nano Today* **2022**, *44*, 101509.

7. W. Fan, P. Huang, X. Chen, *Chem. Soc. Rev.* **2016**, *45*, 6488.

8. G. Li, M. Wu, Y. Xu, Q. Wang, J. Liu, X. Zhou, H. Ji, Q. Tang, X. Gu, S. Liu, Y. Qin, L. Wu, Q. Zhao, *Coord. Chem. Rev.* **2023**, *478*, 214979.

9. D. Zhu, Y. Duo, M. Suo, Y. Zhao, L. Xia, Z. Zheng, Y. Li, B. Z. Tang, *Angew. Chem. Int. Ed.* **2020**, *59*, 13836.

10. N. Kang, S. Son, S. Min, H. Hong, C. Kim, J. An, J. S. Kim, H. Kang, *Chem. Soc. Rev.* **2023**, *52*, 3955.

11. H. Chen, Y. Wan, X. Cui, S. Li, C. S. Lee, *Adv. Healthcare Mater.* **2021**, *10*, e2101607.

12. J.-n. Liu, W. Bu, J. Shi, *Chem. Rev.* **2017**, *117*, 6160.

13. D. Chen, Q. Xu, W. Wang, J. Shao, W. Huang, X. Dong, *Small* **2021**, *17*, e2006742.

14. C. Zhang, X. Hu, L. Jin, L. Lin, H. Lin, Z. Yang, W. Huang, *Adv. Healthcare Mater.* **2023**, *12*, e2300530.

15. X. Su, W. J. Wang, Q. Cao, H. Zhang, B. Liu, Y. Ling, X. Zhou, Z. W. Mao, *Angew. Chem. Int. Ed.* **2022**, *61*, e202115800.

16. T. Klimova, N. S. Chandel, *Cell Death Differ.* **2008**, *15*, 660.

17. J. Yang, L. Bai, M. Shen, X. Gou, Z. Xiang, S. Ma, Q. Wu, C. Gong, *ACS Nano* **2023**, *17*, 11414.

18. G. L. Semenza, *Nat. Rev. Cancer* **2003**, *3*, 721.

19. Q. Sun, Q. Su, Y. Gao, K. Zhou, W. Song, P. Quan, X. Yang, Z. Ge, Y. Zhang, G. He, *Aggregate* **2022**, *4*, e298.

20. K. Chen, P. He, Z. Wang, B. Z. Tang, *ACS Nano* **2021**, *15*, 7735.

21. R. Lin, J. Liu, W. Xu, Z. Liu, X. He, C. Zheng, M. Kang, X. Li, Z. Zhang, H. T. Feng, J. W. Y. Lam, D. Wang, M. Chen, B. Z. Tang, *Adv. Mater.* **2023**, *35*, e2303212.

22. M. Li, J. Xia, R. Tian, J. Wang, J. Fan, J. Du, S. Long, X. Song, J. W. Foley, X. Peng, *J. Am. Chem. Soc.* **2018**, *140*, 14851.

23. E. F. Silva, C. Serpa, J. M. Dabrowski, C. J. Monteiro, S. J. Formosinho, G. Stochel, K. Urbanska, S. Simoes, M. M. Pereira, L. G. Arnaut, *Chem. Eur. J.* **2010**, *16*, 9273.

24. Q. Wan, R. Zhang, Z. Zhuang, Y. Li, Y. Huang, Z. Wang, W. Zhang, J. Hou, B. Z. Tang, *Adv. Funct. Mater.* **2020**, *30*, 2002057.

25. S. Liu, J. Han, Y. Chang, W. Wang, R. Wang, Z. Wang, G. Li, D. Zhu, M. R. Bryce, *Chem. Commun.* **2022**, *58*, 10056.

26. Y. Li, R. Zhang, Q. Wan, R. Hu, Y. Ma, Z. Wang, J. Hou, W. Zhang, B. Z. Tang, *Adv. Sci.* **2021**, *8*, e2102561.

27. L. Zhang, Y. Li, W. Che, D. Zhu, G. Li, Z. Xie, N. Song, S. Liu, B. Z. Tang, X. Liu, Z. Su, M. R. Bryce, *Adv. Sci.* **2019**, *6*, 1802050.

28. S. Kuang, F. Wei, J. Karges, L. Ke, K. Xiong, X. Liao, G. Gasser, L. Ji, H. Chao, *J. Am. Chem. Soc.* **2022**, *144*, 4091.

29. C. Jin, G. Li, X. Wu, J. Liu, W. Wu, Y. Chen, T. Sasaki, H. Chao, Y. Zhang, *Angew. Chem. Int. Ed.* **2021**, *60*, 7597.

30. J. Zhao, X. Zhang, L. Fang, C. Gao, C. Xu, S. Gou, *Small* **2020**, *16*, e2000363.

31. A. W. Sainter, T. A. King, M. R. Dickinson, *J. Biomed. Opt.* **2004**, *9*, 193.

32. D. B. L. Teh, A. Bansal, C. Chai, T. B. Toh, R. A. J. Tucker, G. G. L. Gammad, Y. Yeo, Z. Lei, X. Zheng, F. Yang, J. S. Ho, N. Bolem, B. C. Wu, M. K. Gnanasammandhan, L. Hooi, G. S. Dawe, C. Libedinsky, W. Y. Ong, B. Halliwell, E. K. Chow, K. L. Lim, Y. Zhang, B. K. Kennedy, *Adv. Mater.* **2020**, *32*, 2001459.

33. P. Chinna Ayya Swamy, G. Sivaraman, R. N. Priyanka, S. O. Raja, K. Ponnuvel, J. Shanmugpriya, A. Gulyani, *Coord. Chem. Rev.* **2020**, *411*, 213233.

34. J. Zhao, Y. Gao, R. Huang, C. Chi, Y. Sun, G. Xu, X. H. Xia, S. Gou, *J. Am. Chem. Soc.* **2023**, *145*, 11633.

35. S. Boyde, G. F. Strouse, W. E. Jones, T. J. Meyer, *J. Am. Chem. Soc.* **2002**, *112*, 7395.

36. Y.-C. Wei, S. F. Wang, Y. Hu, L.-S. Liao, D.-G. Chen, K.-H. Chang, C.-W. Wang, S.-H. Liu, W.-H. Chan, J.-L. Liao, W.-Y. Hung, T.-H. Wang, P.-T. Chen, H.-F. Hsu, Y. Chi, P.-T. Chou, *Nat. Photonics* **2020**, *14*, 570.

37. J. Zhao, S. Sun, X. Li, W. Zhang, S. Gou, *ACS Appl. Bio. Mater.* **2020**, *3*, 252.

38. H. Chen, F. Wu, X. Xie, W. Wang, Q. Li, L. Tu, B. Li, X. Kong, Y. Chang, *ACS Nano* **2021**, *15*, 20643.

39. X. Xie, Q. Li, H. Chen, W. Wang, F. Wu, L. Tu, Y. Zhang, X. Kong, Y. Chang, *Nano Lett.* **2022**, *22*, 5339.

40. T. Jia, J. Du, J. Yang, F. Li, X. Fang, G. Chen, *Nano Today* **2023**, *51*, 101932.

41. J. Li, K. Shi, Z. F. Sabet, W. Fu, H. Zhou, S. Xu, T. Liu, M. You, M. Cao, M. Xu, X. Cui, B. Hu, Y. Liu, C. Chen, *Sci. Adv.* **2019**, *5*, eaax0937.

42. J. Liu, R. Zhang, C. Shang, Y. Zhang, Y. Feng, L. Pan, B. Xu, T. Hyeon, W. Bu, J. Shi, J. Du, *J. Am. Chem. Soc.* **2020**, *142*, 7858.

43. L. Xia, X. Kong, X. Liu, L. Tu, Y. Zhang, Y. Chang, K. Liu, D. Shen, H. Zhao, H. Zhang, *Biomaterials* **2014**, *35*, 4146.

44. Y. Zhang, D. Luo, Y. Zhang, Q.-H. Zhang, Q.-Y. Ji, S.-K. Zhou, S. Huang, L.-l. Li, F. Lu, W.-F. Yao, F.-F. Cheng, J.-J. Zhu, L. Zhang, *Chem. Eng. J.* **2023**, *454*, 140489.

45. A. Queen, H. N. Bhutto, M. Yousuf, M. A. Syed, M. I. Hassan, *Semin. Cancer Biol.* **2022**, *86*, 899.

46. Y.-Y. Ling, Y.-J. Kong, L. Hao, Z.-Y. Pan, Z.-W. Mao, C.-P. Tan, *Inorg. Chem. Front.* **2023**, *10*, 3284.

47. G. Li, Y. Wu, G. Shan, W. Che, D. Zhu, B. Song, L. Yan, Z. Su, M. R. Bryce, *Chem. Commun.* **2014**, *50*, 6977.

48. Y. Chen, L. Qiao, L. Ji, H. Chao, *Biomaterials* **2014**, *35*, 2.

49. C. W. T. Leung, Y. Hong, S. Chen, E. Zhao, J. W. Y. Lam, B. Z. Tang, *J. Am. Chem. Soc.* **2013**, *135*, 62.

50. R. Wang, X. Li, J. Yoon, *ACS Appl. Mater. Interfaces* **2021**, *13*, 19543.

51. E. E. Hedlund, P. C. McDonald, O. Nemirovsky, S. Awrey, L. D. E. Jensen, S. Dedhar, *Cancers (Basel)* **2019**, *11*, 1002.

52. N. S. P. de Campos, B. S. Souza, G. Silva, V. A. Porto, G. M. Chalbatani, G. Lagreca, B. Janji, E. R. Suarez, *Cancers (Basel)* **2022**, *14*, 1392.

53. N. Liu, Q. Lin, W. Zuo, W. Chen, S. Huang, Y. Han, X. J. Liang, X. Zhu, S. Huo, *Nanoscale Horiz.* **2023**, *8*, 783.

54. M. S. Baptista, J. Cadet, A. Greer, A. H. Thomas, *Photochem. Photobiol.* **2021**, *97*, 1456.

55. X. Jiang, B. R. Stockwell, M. Conrad, *Nat. Rev. Mol. Cell Biol.* **2021**, *22*, 266.

56. H. Yuan, Z. Han, Y. Chen, F. Qi, H. Fang, Z. Guo, S. Zhang, W. He, *Angew. Chem. Int. Ed.* **2021**, *60*, 8174.

57. J. P. F. Angeli, D. V. Krysko, M. Conrad, *Nat. Rev. Cancer* **2019**, *19*, 405.

58. S. C. Chafe, F. S. Vizeacoumar, G. Venkateswaran, O. Nemirovsky, S. Awrey, W. S. Brown, P. C. McDonald, F. Carta, A. Metcalfe, J. M. Karasinska, L. Huang, S. K. Muthuswamy, D. F. Schaeffer, D. J. Renouf, C. T. Supuran, F. J. Vizeacoumar, S. Dedhar, *Sci. Adv.* **2021**, *7*, eabj0364.

59. Z. Yang, W. Su, X. Wei, S. Qu, D. Zhao, J. Zhou, Y. Wang, Q. Guan, C. Qin, J. Xiang, K. Zen, B. Yao, *Cell Rep.* **2023**, *42*, 112945.

SUPPORTING INFORMATION

Additional supporting information can be found online in the Supporting Information section at the end of this article.